3D-Stereoscopic Analysis of Solar Active Region Loops:
I. SoHO/EIT Observations at Temperatures of 1.0-1.5 MK

Markus J. Aschwanden

Department of Astronomy, University of Maryland, College Park, MD 20742, USA;

e-mail: markus@astro.umd.edu

Jeff Newmark, Jean-Pierre Delaboudinière & EIT Team

NASA/GSFC, Code 683.1, Greenbelt, MD 20771

Werner M. Neupert

Hughes SXT Corp., Lanham, MD 20706

Fabrice Portier-Fozzani

Laboratoire d'Astronomie Spatiale, CNRS, BP 8, 13376 Marseille Cedex 12, France

G. Allen Gary

ES82-Solar Physics Branch, Space Science Laboratory, NASA/MSFC, Huntsville, AL 35812

and

Arik Zucker

ETH, Inst.Astronomy, Häldeliweg 15, CH-8092 Zurich, Switzerland

ABSTRACT

The three-dimensional (3D) structure of solar active region NOAA 7986 observed on 1996 August 30 with the *Extrem-ultraviolet Imaging Telescope (EIT)* onboard the *Solar and Heliospheric Observatory (SoHO)* is analyzed. We develop a new method of *Dynamic Stereoscopy* to reconstruct the 3D geometry of dynamically changing loops, which allows us to determine the orientation of the loop plane with respect to the line-of-sight, a prerequisite to correct properly for projection effects in 3D loop models. With this method and the filter-ratio technique applied to EIT 171 Å and 195 Å images we determine the 3D coordinates $[x(s), y(s), z(s)]$, the loop width $w(s)$, the electron density $n_e(s)$, and the electron temperature $T_e(s)$ as function of the loop length s for 30 loop segments. Fitting the loop densities with an exponential density model $n_e(h)$ we find that the so inferred scale height temperatures, $T_e^\lambda = 1.22 \pm 0.23$ MK, match closely the EIT filter-ratio temperatures, $T_e^{EIT} = 1.21 \pm 0.06$ MK. We conclude that these rather large-scale loops (with heights of $h \approx 50 - 200$ Mm) that dominate EIT 171 Å images are close to thermal equilibrium. Most of the loops show no significant thickness variation $w(s)$, but many exhibit a trend of increasing temperature ($dT/ds > 0$) above the footpoint.

Subject headings: Sun: corona — Sun : X-rays, gamma rays — Sun: EUV

1.   INTRODUCTION

2. STEREOSCOPIC DATA ANALYSIS

2.1. Data Set

The investigated active region is a long-lived coronal structure that was present during several solar rotations, from its apparition in July 1996 until its disappearance in September 1996 (Hudson et al. 1998; Harvey & Hudson 1998; Portier-Fozzani et al.1998), numbered as NOAA 7978, 7981, 7986 during subsequent rotations. We concentrate here on the central meridian transit on 1996 Aug 30, when the dipolar magnetic field structure offered the most favorable perspective to disentangle the "jungle" of nested loops.

An Fe IX/X image recorded with *SOHO/EIT* (Delaboudinière et al. 1995) at a wavelength of 171 Å on 1996-Aug-30, 0020:14 UT, is shown in Fig.1 (top). For stereoscopic correlations we will use also *EIT* images from the previous (1996-Aug-29, 0015:15 UT) and following day (1996-Aug-31, 0010:14 UT). The multi-loop structure of this active region is clearer visible in the high-pass filtered rendering shown in Fig.1 (bottom) The filtered image is simply created by subtracting a smoothed image (with a boxcar average over 3×3 pixels) from the original image. The original (full disk) image has a pixel size of 2.585" and was recorded with an exposure time of 3.5 s. The absolute coordinate system of the full-disk image was established by fitting a circle to the solar limb (at 30 limb positions). The accuracy of the so-defined Sun center position is estimated to be $\sigma_x \approx 1$ pixel$/\sqrt{30} \approx 0.2$ pixel. The offset of the Sun center position (x'_0, y'_0) provided (by an automatic limb fitting routine) in the FITS header of the archive EIT image with respect to our value (x_0, y_0) is found to be $(x'_0 - x_0) = +0.5$ and $(y'_0 - y_0) = -3.9$ pixels. For the solar radius we find a difference of $(r'_0 - r_0) = -1.2$ pixels, yielding a pixel size and uncertainty of $\Delta x = 2.585" \pm 0.004"$.

2.2. Dynamic Stereoscopy Method

In order to analyze the 3-dimensional structure of coronal loops we develop a new technique we might call *"Dynamic Stereoscopy"*, opposed to *"Static Stereoscopy"*, where the solar rotation is used to vary the aspect angle of otherwise *static* structures (e.g. Loughhead, Chen & Wang 1984; Berton & Sakurai 1985; Aschwanden & Bastian 1994a,b; Aschwanden et al. 1995). The innovative feature of this new technique is that spatial structures, e.g. coronal loops, are allowed to evolve dynamically during the time interval over which the stereoscopic correlation is performed.

In the *Dynamic Stereoscopy* method we take advantage of the fact that the global magnetic field is slowly evolving (say during a day) compared with heating and cooling processes in coronal loops. Consequently, the coronal magnetic field $\mathbf{B}(\mathbf{x}, t)$ can be considered as invariant over short time scales, while the confined plasma can flow through "magnetic conduits" in a highly dynamic manner. If a specific coronal fluxtube following a field line $\mathbf{B}(\mathbf{x}, t_1)$ is loaded with bright plasma at time t_1, the same fluxtube may be cooled down at time t_2 (say a day later) and invisible at the same observed wavelength, while heating may occur in an adjacent fluxtube $\mathbf{B}(\mathbf{x} + \Delta\mathbf{x}, t_2)$, which was dark at time t_1 and appears now bright at time t_2. For adjacent fluxtubes, the two field lines $\mathbf{B}(\mathbf{x})$ and $\mathbf{B}(\mathbf{x} + \Delta\mathbf{x})$ will run almost parallel, a property we will exploit in our *dynamic stereoscopy* method. Our method is applicable to coronal structures that meet the following two conditions:

1. The global magnetic vector field $B(\mathbf{x}, t)$ is static (or slowly-varying) during the time interval over which stereoscopic correlations are performed (typically 1 day). The magnetic field can be traced out by optically-thin emission (e.g. in soft X-ray or EUV wavelengths).

2. At least one footpoint of an observed coronal loop is identifiable, which can be used as a reference level of the altitude. For EUV emission we assume that the altitude of a loop footpoint is located in the lower corona above the chromosphere, at an altitude of $h_{foot} \approx 2500$ km above the photosphere.

We outline briefly the numerical procedure of our implementation of the *dynamic stereoscopy* method, while the mathematical coordinate transformations are given in Appendix A. The projected geometry of a loop segment in an image at time t_1 is traced out by a series of image coordinates $(x_i, y_i), i = 1, ..., n$, starting at footpoint position (x_1, y_1), assumed to be anchored at height h_{foot} (Fig.2). Two additional variables to characterize the 3D geometry of the loop segment are the azimuth angle α of the footpoint baseline, and the inclination angle ϑ of the mean loop plane (intersecting the footpoint baseline, see Fig.2). The procedure of stereoscopic correlation (illustrated in Fig.3) includes the following steps:

1. Measuring of positions $(x_i, y_i), i = 1, ..., n_j$ by tracing a loop segment in an image recorded at time t_1, starting with the primary footpoint at (x_1, y_1).

2. Estimating the position of the secondary footpoint (x_{F2}, y_{F2}) to obtain the azimuth angle α of the footpoint baseline. If the full length of the loop can be traced, the secondary footpoint is just given by the last point x_n, y_n, and the tangens of the azimuth angle α corresponds to the ratio of the latitude $(b_{F_2} - b_{F_1})$ and longitude difference $(l_{F_2} - l_{F_1})$ of the two footpoints, i.e.

$$\tan(\alpha) = \frac{(b_{F_2} - b_{F_1})}{(l_{F_2} - l_{F_1})} . \tag{1}$$

However, most of the loops analyzed here extend over several density scale heights, so that only a segment above the primary footpoint can be traced out, while the location of the secondary footpoint has to be estimated based on the general dipole characteristic of the ambient magnetic topology. We repeat the localization of the secondary footpoint 5 times and obtain from these estimates $\alpha_j, j = 1, ..., 5$ a mean and standard deviation $\alpha \pm d\alpha$.

3. The loop positions (x_i, y_i) measured in the image at time t_1 are then transformed into heliographic longitude and latitude coordinates (l_{ij}, b_{ij}) and altitudes (h_{ij}), based on the azimuth angle α of the footpoint baseline and the variable inclination angle ϑ_j, which is varied over a range of $-90^0 < \vartheta_j < +90^0$ in increments of $\Delta\vartheta = 1^0$.

4. The heliographic coordinate $l_{ij}(t_1)$ is then transformed to the time t_2 of the second stereoscopic pair image, $l'_{ij}(t_2)$, using the solar differential rotation rate applied to the time interval $(t_2 - t_1)$. We use the differential rotation rate specified by Allen (1973),

$$l'(t_2) = l(t_1) + [13.45^0 + 3^0 \sin^2(B)]\frac{(t_2 - t_1)}{1 \text{ day}} . \tag{2}$$

The heliographic latitude b_{ij} and altitude h_{ij} are assumed to be constant during the considered time interval.

5. In the stereoscopic pair image at time t_2 we calculate the image coordinates (x'_{ij}, y'_{ij}) of the projected loop structure. Parallel to these loop curves (with typical lengths of $n_s = 50 - 200$ pixels) we extract image stripes of some width ($n_w = 16$ pixels) by interpolating the image brightness $F(x, y)$ at the positions of the curved coordinate grid.

6. The stretched 2D image stripes ($n_s \times n_w$ pixels) are then scanned for parallel brightness ridges, caused by "*dynamic*" structures that are co-aligned (or parallel-displaced) to the loop projection in image t_2 (for illustration see examples shown in lower panels of Fig.3). This scanning process is numerically performed by measuring the total length $L(\vartheta_k)$ of coaligned brightness ridges that are detected in each stripe k associated with each angle ϑ_j. The maximum of this quantity ($max[L(\vartheta_k)]$) is used to infer the most likely value of the inclination angle ϑ of the loop plane.

7. The same procedure is repeated in forward and backward direction in time. The mean and standard deviation of $\vartheta \pm d\vartheta$ is determined by averaging the two stereoscopic solutions (± 1 day).

The independent stereoscopic correlation in forward ($+1$ day) and backward (-1 day) direction provides a useful redundancy of the solution. The time difference of ± 1 day corresponds to an aspect angle change of $\pm 13.5^0$. Except for steps 1-2, which constitute the definition of a selected loop feature, all other steps (3-7) of the stereoscopic correlation are performed automatically by a numeric code without human interaction. The determination of the loop inclination angle ϑ is therefore achieved in a most objective way, within the principle of *dynamic stereoscopy*.

2.3. Loop Geometry

With the dynamic stereoscopy method described above we analyzed the 3-dimensional (3D) coordinates of 30 loops from the *EIT* 171 Å image on 1996-Aug-30 (Fig.4, middle column). The true 3D geometry of (the central axis) of a coronal loop can be characterized with three orthogonal spatial coordinates $[x(s_i), y(s_i), z(s_i)], i = 1, ..., n$, parametrized by the loop length parameter s_i. When we trace a loop structure in an image (see Fig.4, panels in middle column), we can accurately measure the two coordinates $[x(s_i), y(s_i)]$, without imposing any geometric constraint on its shape, opposed to a method that fits a predefined geometric model (e.g. an elliptic projection of a circular geometry). We impose only some constraints on the third coordinate $z(s_i)$, namely assuming that the loop segment is confined into a plane, whose orientation we quantify with two free parameters (Fig.2): with the azimuth angle α (of the loop footpoint baseline) and the inclination angle ϑ (with respect to the vertical). One additional constraint is also introduced by the reference level $h(s_1)$ of the first footpoint position, assumed to be located at a fixed height of $h(s_1) = h_{foot} \approx 2.5$ Mm.

Some geometric elements of the analyzed 30 loops are listed in Table 1: the heliographic longitude (l_1) and latitude (b_1) position of the primary footpoint $[x(s_1), y(s_1), h(s_1) = h_{foot}]$, the azimuth angle α of the footpoint baseline measured at the primary footpoint, and the inclination angle ϑ of the loop plane. The average heliographic position of the 30 loop footpoints is $< l_{F_1} > = 251.0^0, < b_{F_1} > = -11.8^0$, which is slightly southward of the Sun center position at this time, $l_0 = 255.8^0, b_0 = 7.2^0$.

The average azimuth angle (modulo 180^0) of the 30 loop footpoint baselines is $\alpha = -3^0 \pm 10^0$, which represents the global orientation of the large-scale dipolar magnetic field that dominates the active region, that was used as a guide to estimate the azimuth angle of the footpoint baseline for indiviudal loop segments. The only complete loop that could be traced out (without gaps between the footpoints) is Loop #1, which has an azimuth angle of $\alpha = 15^0 \pm 1^0$.

The inclination angles ϑ of the loop planes cover a large range from $\vartheta = -56^0$ to $\vartheta = +69^0$, having an average of $< \vartheta > = 7^0 \pm 37^0$. The southern loops (Loops #1-11, 23-30) show all an inclination toward south (with ϑ negative if the primary footpoint is to the East), while the northern loops (Loops #12-22)

show a systematic inclination toward North (with ϑ positive if the primary footpoint is to the East). This fan-shaped divergence of loop planes is consistent with the overall magnetic dipolar field, having the dipole axis aligned to the East-West direction.

We visualize the 3D structure of the stereoscopically reconstructed 30 loops in Fig.5, where different perspectives and viewing angles are displayed. The traced segments (Fig.4) of the reconstructed loops are marked with thick lines in Fig.5, while the thin lines represent circular segments in the loop plane, constrained by the two footpoints and the endpoint of the traced segment. We rotated these reconstructed 30 loops by -7.2 days to the East (Fig.5 bottom left), in order to illustrate the distribution of inclination angles. The group of loops that are inclined to the South in our EIT image of 1996-Aug-30, are also found to have a similar configuration (with similar loop heights and loop plane inclinations) in an EIT image observed 7.2 days earlier, when this active region crosses the East limb (Fig.5 top left).

2.4. Loop Background Subtraction

We parametrize the positions of the traced loop segments from the image coordinates $[x(s_i), y(s_i)]$ as function of the (projected) loop length parameter s_i, by interpolating the coordinates with a constant resolution of $\Delta s = s_{i+1} - s_i = 1$ pixel in the image plane. These positions mark the central axes of the analyzed loops. For single-loop analysis it is convenient to introduce a coordinate grid $[s_i, t_j]$ that is stretched out along the loop axis, with t_j a coordinate orthogonal to the loop axis. The projections $[x(s_i, t_j), y(s_i, t_j)]$ of these curved coordinate grids are shown in Fig.6 (top right panel). We parameterized both coordinates $[s_i, t_j]$ with a uniform resolution of 1 pixel, and have chosen a width of 16 pixels for the width of the stripes (t_j), symmetrically bracketing the central loop axis. We show the flux $F(t_j)$ as function of the loop cross-section t_j for each loop (#1–30), and for each position s_i along the central loop axis with a step of $\Delta s_i = 1$ pixel in Fig.6, measured from the EIT 171 Å image of 1996-Aug-30.

In a next step we attempt to separate the loop-associated fluxes from the loop-unrelated background. This is a very crucial step to determine the correct emission measure and electron density in a given loop. This task is difficult because most of the loops are very closely spaced and separated only by a few pixels at their primary footpoint (see Fig.6). Very few loops occur in an isolated environment (e.g. such as loop #25, see Figs.4-6). For many cross-sections there is not enough separation between adjacent loops to model the loop-unrelated background properly. The fact that the flux-unrelated background makes up typically 50-90% of the total EUV flux measured at the same position (see Fig.7), indicates that we can separate out only a fraction of super-imposed and nested loops, like the top-most elements on the topological surface of a "strang of spaghettis". We tested various methods and found the following to be least susceptible to confusion by adjacent loops. We calculated the background profile $F_B(t_j)$ to the observed flux $F(t_j)$ by cubic spline interpolation between various intervals $[t_1, t_2]$, which were varied over a range of $t_0 - t_1 = 1...4$ and $t_2 - t_0 = 1...4$ pixels (or 2-7 Mm for the half width of the loop cross-section) on both sides of the central loop axis (at t_0). From the varied loop boundaries $[t_1, t_2]$ we select those values for the best background estimate that maximize the flux of the loop cross-section, i.e. which yield the maximum of $\int [F(t_j) - F_B(t_j)] dt_j$. This method has the advantage to adjust for loop thickness variations, for offsets in tracing of the central axis, and for co-alignment errors between the 171 and 195 Å image in the use of the filter-ratio technique. The so-determined loop-associated fluxes are shown with grey areas for each cross-section $F(t_j)|_{s=s_i}$ in Fig.6. The results show that the allowed loop half-width range of $\pm 1 - 4$ pixels separates most of the loops reasonably, except for occasional double loop detections near the primary footpoint. Such loop segments where the loop separation fails will be excluded in further analysis.

2.5. Loop Cross-Sections

We measured the loop width $w(s)$ as function of the loop length parameter s, using the definition of the *equivalent width* $w(s)$,

$$w(s) = \frac{\int F(s,t_j) - F_B(s,t_j) \; dt_j}{max[F(s,t_j) - F_B(s,t_j)]} \; . \tag{3}$$

These loop widths $w(s)$ are shown as function of the loop length s in Fig. 8 for the 10 loops that are least confused by adjacent loops, as it can be judged from the cross-sections $F(t_j)|_{s=s}$, shown in Fig.6 (Loop #1, 8, 11, 14, 15, 19, 20, 21, 25, 28). Performing a linear regression fit to the observed values $w(s)$ we find a significant variation of the loop thickness only for two of them (Loop #20 and 28). To quantify the variation of the loop thickness we calculated a *loop divergence factor*, defined by the average width in the upper part $(s_{max}/2 < s < s_{max})$ to the lower part $(0 < s < s_{max}/2)$ of the traced loop segment. We remind that the traced loop segments generally extend over about one density scale height, but do often not reach the loop top (except for the smallest loop, #1). The loop divergence factors and their uncertainties are shown in Fig.8 (bottom right panel) for each loop. We caution that some of the loop thickness variation near the footpoints is due to separation problems of closely-spaced adjacent loops (as it can be judged from Fig.6). A histogram of average loop widths is shown in Fig.8 (top right panel), while the individual values w and their mean and standard deviation ($w = 7100 \pm 800$ km) is also listed in Table 1. The preference for such a narrow range of loop diameters is perhaps an instrumental resolution bias, because the finest recognizable structures are most likely to be seen at a scale corresponding to the size of a few pixels.

2.6. Loop Densities and Scale Heights

For electron density and temperature diagnostics we are using a filter ratio technique applied to the EIT 171 Å and 195 Å wavelength images, based on the most recent EIT standard software (status of February 1989). The resulting emission measures EM and temperatures T_e^{EIT} are based on the calculation of synthetic spectra using the *CHIANTI* data base, containing some 1400 emission lines in the 150-400 Å wavelength range. Comparing these current standard values (as referred to in this study) with recent new calibration data obtained from a rocket flight with a duplicate EIT instrument (led by Dan Moses, NRL), the emission measure values quoted here would have to be corrected by $\approx -20\%$, or the electron density by $\approx -40\%$, respectively, while the temperature values remain basically unchanged.

To determine the electron density $n_e(s)$ along individual loops, we use the background-subtracted EIT fluxes $F_{loop}(s) = F(s) - F_B(s)$ in the filter ratios and the loop widths $w(s)$. An additional important loop parameter is the line-of-sight angle $\psi(s)$, which provides a correction factor of the effective column depth for a loop with circular cross-section specified by a diameter $w(s)$, i.e. $w_z(s) = w(s)/\cos[\psi(s)]$ (see Appendix B). With this parameterization we define the density $n_e(s)$ along a loop by

$$n_e(s) = \sqrt{\frac{EM(s)}{w_z(s)}} = \sqrt{\frac{EM(s) \; \cos[\psi(s)]}{w(s)}} \; , \tag{4}$$

with the loop length $s(x,y)$ parametrized as a function of the image position (x,y), from where the EIT emission measure $EM(x,y)$ is measured. Because the line-of-sight angle $\psi(s)$ is very sensitive to the loop orientation, correct values of the electron density $n_e(s)$ can only be obtained from an appropriate 3D model of the loop (constrained by stereoscopic correlations here). The projection effect of the loop curvature on

the effective column depth $w_z(s)$, and the effect of the inclination angle ϑ of the loop plane on the inferred density scale height $\lambda(\vartheta)$ are illustrated in Fig.9.

The electron density $n_e(s)$ calculated from Eq.4 is shown graphically for the 10 least-confused loops (# 1,8,11,14,15,19,20,21,25,28) in Fig.10 (left panels). Because the height dependence $s(h)$ of the loop length is known from our stereoscopic reconstruction (displayed in Fig.5), we can directly obtain the parametrization $n_e[s(h)] \mapsto n_e(h)$ and fit an exponential density model,

$$n_e(h) = n_{e0} \, \exp(-\frac{h}{\lambda(T_e)}) \tag{5}$$

to obtain a scale-height temperature T_e^λ, which is defined by (e.g. Lang 1980, p.285)

$$\lambda(T_e) = \frac{k_B T_e}{\mu \, m_H g} \approx 46(\frac{T_e}{1MK}) \text{ [Mm] ,} \tag{6}$$

with k_B the Boltzmann constant, μ the mean molecular weight ($\mu \approx 1.4$ for the solar corona), m_H the mass of the hydrogen atom, and g the acceleration of gravity at the solar surface. The so obtained scale heights λ, with a mean of $\lambda = 55 \pm 10$ Mm, and the inferred scale height temperatures T_e^λ, with a mean of $T_e^\lambda = 1.22 \pm 0.23$, are listed in Table 1 for each of the analyzed 30 loops. Loop segment ranges that are obviously confused by adjacent or crossing loops (as it can be judged from Fig.6), have been excluded in the fitting of the scale height model. We find that most of the analyzed loop segments fit closely an exponential density model (see Fig.10 left). Deviations from an exponential density model can often be explained by uncertainties in the background subtraction, or by confusion from adjacent or overlying loops.

2.7. Loop Temperatures

Independently of the scale height temperature T_e^λ, we can also determine the temperature directly from the EIT filter ratio, which moreover provides a temperature differentiation along the loop, $T_e^{EIT}(s)$. Since our loop definitions are based on tracing of EIT 171 Å image, we use only the filter ratio of EIT 171 Å (Fe IX,X) and 195 Å (Fe XII), which is sensitive in the temperature regime of $T_e = 1.0 - 1.5$ MK. We are using the spatial loop definition $[x(s), y(s)]$ based on the 171 Å image, and apply the same background-subtraction technique to the 195 Å image, before we determine the temperature from the filter ratio $(F^{171} - F_B^{171})/(F^{195} - F_B^{195})$. Because our background-subtraction technique has some tolerance (of $\pm 1 - 4$ pixels) in the localization of the loop cross-section (by maximizing the flux integrated over the loop cross-section), the filter-ratio is not susceptible to small co-alignment errors between the 171 and 195 Å image. The employed background-subtraction technique requires also a correlated structure (with a width of 2-8 pixels) in both wavelengths, while larger or diffuse structures with possibly different temperatures are safely subtracted out.

The filter-ratio temperatures T_e^{EIT} averaged over the loop segments are tabulated in Table 1, with a mean of $T_e^{EIT} = 1.21 \pm 0.06$ MK. The distribution of filter-ratio temperatures $N(T_e^{EIT})$ is shown in Fig.11 (bottom left), along with the distribution of scale height temperatures $N(T_e^\lambda)$ (Fig.11 top left), which have almost identical means. The range of scale height temperatures (± 0.23 MK) is broader than the range EIT filter-ratio temperatures (± 0.06 MK), probably because of systematic errors in background subtraction and loop separation. This is also consistent with the scatterplot of the two temperature definitions (Fig.11 top right), where no obvious correlation is seen. Despite of these unavoidable uncertainties in the background subtraction, it is remarkable that the means of the two independently determined temperatures conincides so closely.

2.8. Loop Temperature Gradients

The detailed variation of the temperature $T_e^{EIT}(s)$ along the loop length s is shown for the 10 least-confused loops in Fig.10 (right panels). We note that the filter-ratio temperature varies sometimes discontinously along the loop, e.g. there is a jump from $T_e = 1.35$ MK to $T_e = 1.1$ MK at $s = 70$ Mm in Loop #1 (Fig.10, top right), which may be caused by contamination from a hotter loop that is located almost parallel to Loop #1 at $s < 70$ Mm (see cross-sections in Fig.6). Such confusion problems can only be identified in hindsight. Despite of such confusion problems, there seems to be a trend of a positive temperature gradient $dT/ds > 0$ above the footpoint. To estimate these average temperature gradients (without correcting for multi-loop confusion) we performed a linear regression $T_e(s)$ for all loops. Most significant temperature gradients are found for Loop #11 ($dT/ds = +0.0049$ MK/Mm), for Loop #20 ($dT/ds = +0.0012$ MK/Mm), and for Loop #25 ($dT/ds = +0.0054$ MK/Mm). The distribution of temperature gradients $N(dT/ds)$ is shown in Fig.11 (bottom right), revealing that $\approx 75\%$ of the loops have a positive temperature gradient $dT/ds > 0$ within the first scale height above their footpoints. Higher parts ($h \gtrsim 1\lambda$) of these loops are not detectable in EIT images due unsufficient density contrast (one scale height corresponds to a factor of ≈ 3 in density or a factor of ≈ 10 in emission measure or EIT flux).

3. PHYSICAL INTERPRETATION AND DISCUSSION

4. CONCLUSIONS

A. (APPENDIX) Heliographic Coordinate Systems and Transformations

For analysis of observed images, for time-dependent coordinate transformations that take the solar rotation into account (as needed in stereoscopic correlations), and for convenient definitions of loop geometries we define 3 different coordinate systems:

Image Coordinate System (x,y,z): The (x, y) coordinates refer to the x-axis and y-axis of an observed image, while the coordinate (z) is orthogonal to the image, or parallel to the line-of-sight direction, defined positive toward the observer. The origin $(x, y, z) = (0, 0, 0)$ of this coordinate system is most conveniently assumed at the Sun center position. A solar FITS image should contain the position of the Sun center in pixel units (i_{x0}, j_{y0}) (in FITS header $CRPIX1$, $CRPIX2$ or E_XCEN, E_YCEN), the pixel size $(\Delta x, \Delta y)$ in units or arcseconds (in FITS header $CDELT1$, $CDELT2$), and the solar radius i_{r0} in pixel units (in FITS header $SOLAR\_R$, or E_XSMD, E_YSMD if the semi-diameters of an ellipse are fitted). With this information, a pixel position (i, j) can then be converted into the coordinate system (x, y) by

$$x_i = \Delta x \; (i - i_{x0}) \tag{A1}$$

$$y_i = \Delta y \; (j - j_{x0}) \; , \tag{A2}$$

where Δx=arcseconds/pixel for (x, y) in units of arcseconds, or $\Delta x = R_{\odot}/i_{r0}$, with $R_{\odot} = 696,000$ km, if physical length units (km) are preferred.

Heliographic Coordinate System (l,b,r): The heliographic coordinate system is co-rotating with the solar surface. A position on the solar surface is generally specified by heliographic longitude and latitude coordiantes (l, b) (in units of heliographic degrees), with reference to the _Carrington rotation_ grid. The heliographic longitude and latitude $[l_0(t), b_0(t)]$ of the Sun center and the position angle $P(t)$ of the solar rotation axis for a given time t are published in _The Astronomical Almanach_ (Nautical Almanac Office, NRL, Washington DC). The 2-dimensional spherical coordinate system (l, b) can be generalized into a 3-dimensional coordinate system by incorporating the height h above the solar surface, which can be expressed as a dimensionless distance to the Sun center (in units of solar radii),

$$r = (1 + \frac{h}{R_{\odot}}) \; . \tag{A3}$$

The transformation from the 3D heliographic coordinate system (l, b, r) into image coordinates (x, y, z) can be accomplished by applying a series of 4 rotations to the (normalized) vector $(0, 0, r)$,

$$
\begin{pmatrix} x/R_{\odot} \\ y/R_{\odot} \\ z/R_{\odot} \end{pmatrix} =
\begin{pmatrix} \cos(P+P_0) & -\sin(P+P_0) & 0 \\ \sin(P+P_0) & \cos(P+P_0) & 0 \\ 0 & 0 & 1 \end{pmatrix}
\begin{pmatrix} 1 & 0 & 0 \\ 0 & \cos(b_0) & -\sin(b_0) \\ 0 & \sin(b_0) & \cos(b_0) \end{pmatrix}
$$
$$
\begin{pmatrix} \cos(l_0 - l) & 0 & -\sin(l_0 - l) \\ 0 & 1 & 0 \\ \sin(l_0 - l) & 0 & \cos(l_0 - l) \end{pmatrix}
\begin{pmatrix} 1 & 0 & 0 \\ 0 & \cos(-b) & -\sin(-b) \\ 0 & \sin(-b) & \cos(-b) \end{pmatrix}
\begin{pmatrix} 0 \\ 0 \\ r \end{pmatrix} \; , \tag{A4}
$$

where (l_0, b_0) are the heliographic longitude and latitude of the Sun center, P is the position angle of the solar rotation axis with respect to the North-South direction (defined positive towards East), and P_0 is the image rotation (roll) angle with respect to the North-South direction, $(P + P_0 = 0$ for images rotated to solar North). In stereoscopic correlations, only the longitude of the Sun center, $l_0(t)$, is time-dependent in first order (according to the solar rotation rate), while $b_0(t)$ and $P(t)$ are slowly-varying, and thus almost constant for short time intervals.

Loop Plane Coordinate System (X,Y,Z): To parametrize coronal loops it is also convenient to introduce a cartesian system that is aligned with the loop footpoint baseline (X-axis) and coincides with the loop plane (X–Z plane, $Y = 0$). The transformation of loop coordinates $(X, Y = 0, Z)$ into cartesian coordinate system (X', Y', Z') that is aligned with the heliographic coordinate system (l, b, r) can simply be accomplished with help of two rotations,

$$
\begin{pmatrix} X' \\ Y' \\ Z' \end{pmatrix} = \begin{pmatrix} \cos(\alpha) & -\sin(\alpha) & 0 \\ \sin(\alpha) & \cos(\alpha) & 0 \\ 0 & 0 & 1 \end{pmatrix} \begin{pmatrix} 1 & 0 & 0 \\ 0 & \cos(\vartheta) & \sin(\vartheta) \\ 0 & -\sin(\vartheta) & \cos(\vartheta) \end{pmatrix} \begin{pmatrix} X \\ Y \\ Z \end{pmatrix} , \tag{A5}
$$

where the *azimuth angle* α denotes the angle between the loop footpoint baseline and the East-West direction, and ϑ represents the inclination or tilt angle between the loop plane and the vertical to the solar surface (Fig.2). Placing the origin of the loop coordinate system $[X = 0, Y = 0, Z = 0]$ (which is also the origin of the rotated coordinate system $[X' = 0, Y' = 0, Z' = 0]$ at heliographic position (l_1, b_1) at an altitude h_{Foot} above the solar surface, the transformation into heliographic coordinates is then given by

$$
\begin{pmatrix} l \\ b \\ r \end{pmatrix} = \begin{pmatrix} l_1 + \arctan[X'/(Z' + h_{Foot} + R_\odot)] \\ b_1 + \arctan[Y'/(Z' + h_{Foot} + R_\odot)] \\ \sqrt{[X'^2 + Y'^2 + (Z' + h_{Foot} + R_\odot)^2]}/R_\odot \end{pmatrix} . \tag{A6}
$$

A semi-circular loop (with radius R_0) can then be defined in this loop plane (X, Y, Z) simply by

$$
\begin{pmatrix} X \\ Y \\ Z \end{pmatrix} = \begin{pmatrix} R_0 \cos(\varphi) \\ 0 \\ R_0 \sin(\varphi) \end{pmatrix} , \tag{A7}
$$

where the loop length $s = R_0\varphi$ can be parametrized with one single parameter (φ).

B.   (APPENDIX) Line-of-Sight Correction on Loop Column Depth

Column depth of loops with constant cross-section: In order to convert observed emission measures $EM(x, y) = \int n_e^2(x, y, z)dz$ into local electron densities $n_e(x, y, z)$ we need information on the column depth $\int dz$. An approximation that is often useful are coronal loops with a constant cross-section w, which can be measured from the FWHM as it appears perpendicular to the line-of-sight in the plane of the sky. For 3-dimensional models of loops parametrized by coordinates (x_i, y_i, z_i), the angle ψ between the line-of-sight and a loop segment can then directly be derived by the ratio of the projected to the effective length of a loop segment $[i, i + 1]$.

$$
\cos(\psi[x_i, y_i, z_i]) = \frac{\sqrt{(x_{i+1} - x_i)^2 + (y_{i+1} - y_i)^2}}{\sqrt{(x_{i+1} - x_i)^2 + (y_{i+1} - y_i)^2 + (z_{i+1} - z_i)^2}} \tag{B1}
$$

yielding the column depth w_z along the line-of-sight axis z,

$$
w_z[x_i, y_i, z_i] = \frac{w}{\cos(\psi[x_i, y_i, z_i])} . \tag{B2}
$$

C. REFERENCES

Alexander.D. and Katsev,S. 1996, SP 167, 153

Allen,C.W. 1973, Astrophysical Quantities, London:Athlone

Antonnucci,E., Gabriel,A.H., and Dennis,B.R. 1984, ApJ 287, 917

Aschwanden,M.J. 1995, Lecture Notes in Physics 444, 13

Aschwanden,M.J. and Bastian,T.S. 1994a, ApJ 426, 425

Aschwanden,M.J. and Bastian,T.S. 1994b, ApJ 426, 434

Aschwanden,M.J., Bastian,T.S., Nitta,N., Newmark,J., Thompson,B.J. and Harrison,R.A. 1998, in Proc. 2nd Advances in Solar Physics Euroconference (ASPE), Three-Dimensional Structure of Solar Active Regions, (eds. C.Alissandrakis and B.Schmieder), PASP, subm.

Aschwanden,M.J., Bastian,T.S. and White,S.M. 1992, Proc. of the 1st SOHO Workshop, Annapolis, Maryland, USA, 25-28 August 1992, ESA SP-348, p.217

Aschwanden,M.J., Lim,J., Gary,D.E., and Klimchuk,J.A. 1995, ApJ 454, 412

Aschwanden,M.J., Neupert,W.N., Newmark,J., Thompson,B.J., Brosius,J.W., Holman,G.D., Harrison,R.A., Bastian,T.S., Nitta,N., Hudson,H.S., and Zucker,A. 1998, in Proc. 2nd Advances in Solar Physics Euroconference (ASPE), Three-Dimensional Structure of Solar Active Regions, (eds. C.Alissandrakis and B.Schmieder), PASP, subm.

Bastian,T.S. 1994, ApJ 426, 774

Bastian,T.S. 1995, ApJ 439, 494

Berton,R. and Sakarai,T. 1985, SP 96, 93

Bray,R.J., Cram,L.E., Durrant,C.J., and Loughhead, R.E. 1991, Plasma Loops in the Solar Corona, Cambridge: Cambridge University Press

Brosius,J.W., Davila,J.M., Thomas,R.J., Saba,J.L.R., Hara,H. and Monsignori-Fossi,B.C., 1996, ApJ 477, 969

Brosius,J.W., Davila,J.M., Thomas,R.J., and Monsignori-Fossi,B.C. 1996, ApJS 106, 143

Brosius,J.W., Davila,J.M., Thomas,R.J., and Thompson,W.T. 1994, ApJ 425, 343

Brosius,J.W., Davila,J.M., Thompson,W.T., Thomas,R.J., Holman,G.D., Gopalswamy,N., White,S.M., Kundu,M.R., and Jones,H.P. 1993, ApJ 411, 410

Brosius,J.W., and Holman,G.D. 1988, ApJ 327, 417

Brosius,J.W., Willson,R.F., Holman,G.D., and Schmelz,J.T. 1992, ApJ 386, 347

Cargill,P. 1992, in J.L.Birch and J.H.Waite,Jr. (eds.), Solar System Plasma Physics: Resolution of Processes in Space and Time, Proc. Yosemite Conf.

Davila,J.M. 1987, ApJ 317, 514

Delaboudinière,J.P., et al. 1995, SP 162, 291

Falconer,D.A., Moore,R.L., Poerter,J.G., Gary,G.A. and Shimizu,T. 1997, ApJ 482, 519

Forbes,T.G. 1991, *Geophys. Astrophys. Fluid Dynamics*, 62, 13

Galeev,A.A., Rosner,R., and Vaiana,G.S. 1979, ApJ 229, 318

Gary,A. 1997, SP 174, 241

Gary,A. 1989, ApJS 69, 323

Gary,A., Moore,R., Hagyard,M., and Haisch,B., 1987, ApJ 314, 782

Gary,A., and Demoulin,P. 1995, ApJ 445, 982

Gomez,D.O. 1990, *Fund. Cosmic Physics* 14, 131

Harvey,K.L. and Hudson,H.S. 1998, in "Observational Plasma Astrophysics: Five Years of Yohkoh and Beyond", Proc. Yohkoh Workshop, Yoyogi, Tokyo, Japan, Nov. 6-8, 1996, (eds. T.Watanabe, T.Kosugi, and A.C.Sterling), in press

Heyvaerts,J. 1990, in E.R.Priest and V.Krishnan (eds.), *Basic Plasma Processes on the Sun*, IAU Symp. 142, 207

Hollweg,J.V. 1991, in P.Ulmschneider, E.R.Priest, and R.Rosner (eds.), *Mechanisms of Chromospheric and Coronal Heating*, Berlin:Springer, p.423

Holman,G.D. 1994, in Proc. *XIVth NSO/Sacramento Peak Summer Workshop*, (eds. Balasubramaniam,K.S., and Simon,G.W.), PASP 68, 356

Hudson,H.S. 1991, Solar Phys. 133, 357

Hudson,H.S., LaBonte,B.J., Sterling,A.C., and Watanabe,T. 1998, in "Observational Plasma Astrophysics: Five Years of Yohkoh and Beyond", Proc. Yohkoh Workshop, Yoyogi, Tokyo, Japan, Nov. 6-8, 1996, (eds. T.Watanabe, T.Kosugi, and A.C.Sterling), in press

Kano,R. and Tsuneta,S. 1995, ApJ 454, 934

Klimchuk,J.A., 1992 in *Coronal Streamers, Coronal Loops, and Coronal and Solar Wind Composition*, (eds. V.Domingo, A.Poland, and J.Mariska), ESA SP-348, 167

Klimchuk,J.A., and Gary,D.E. 1995, ApJ 448, 925

Klimchuk,J.A., Lemen,J.R., Feldman,U., Tsuneta,S., and Uchida,Y. 1992, PASJ 44, L181

Klimchuk,J.A. and Porter,L.J. 1995, Nature, 377, 131

Krucker,S., Benz,A.O., Bastian,T.S., and Acton,L.W. 1997, ApJ 488, 499

Krucker,S., Benz,A.O., and Delaboudinière,J.P. 1997, Nature, subm.

Lang,K.R. 1980, Astrophysical Formulae, Berlin:Springer

Litwin,C. and Rosner,R. 1993, ApJ 412, 375

Loughhead,R.E., Wang,J.L., and Blows,G. 1983, ApJ 274, 883

Loughhead,R.E., Chen,C.L., and Wang,J.L. 1984, SP 92, 53

Mikic,Z., Schnack,D.D., and VanHoven,G. 1989, ApJ 338, 1148

Moses, J.D., Newmark, J.S., et al. (1997), SP, in press

Neupert,W.M. 1967, SP 2, 94

Neupert et al. 1998, SP, in preparation

Neupert,W.M., Brosius,J.W., Thomas,R.J., and Thompson,W.T. 1992, SP 137, 87

Neupert,W.M., Newmark,J., Thompson,B.J., Catura,R., Moses,J.D., Portier-Fozzani,F., Delaboudinière,J.P., Gabriel,A., Artzner,G., Clette,F., Cugnon,P., Maucherat,A., Defise,J.M., Jamar,C., Rochus,P., Howard,R., Michels,D., Dere,K., Freeland,S., Lemen,J., Stern,R. and Gurman,J. 1997, presented at SPD Meeting, Bozeman/Montana

Newmark, J.S., et al. (1997), EOS Trans., SH22A-08

Newmark, J.S., et al. (1996), EOS Vol. 77, No. 46, 557

Nitta, N., White, S.M., Kundu, M.R., Gopalswamy, N., Holman, G.D., Brosius, J.W., Schmelz, J.T., Saba, J.L.R., and Strong, K.T. 1991, ApJ 374, 374

Ofman,L., Davila,J.M., and Steinolfson,R.S. 1994, ApJ 421, 360

Parker,E.N. 1988, ApJ 330, 474

Peres,G. 1997, in 5th SOHO Workshop on the corona and solar wind near Minimum Activity, ESA SP-404, in press

Pneuman,G.W. 1981, in *Solar Flare Magnetohydrodynamics*, ed. E.R.Priest (New York: Gordon & Breach), p.379

Porter,L.J. and Klimchuk,J.A. 1995, ApJ 454, 499

Portier-Fozzani,F., Neupert,W., Aschwanden,M.J., Sheeley,N.R., Thompson,B., Maucherat,A.J., Newmark,J., Klimchuk,J., and EIT Team 1998, in Proc. 2nd *Advances in Solar Physics Euroconference (ASPE), Three-Dimensional Structure of Solar Active Regions*, (eds. C.Alissandrakis and B.Schmieder), PASP, subm.

Press,W.H., Flannery,B.P., Teukolsky,S.A., and Vetterling,W.T. 1986, *Numerical Recipes, The Art of Scientific Computing*, Cambridge: Cambridge University Press

Priest,E.R. 1985, Rep.Prog.Phys. 48, 955

Rosner,R., Tucker,W.H., and Vaiana,G.S. 1978, ApJ 220, 643

Rosner,R., and Vaiana,G.S. 1977, ApJ 216, 141

Scudder,J. 1993a, ApJ 398, 299

Scudder,J. 1993b, ApJ 398, 319

Serio,S., Peres,G., Vaiana,G.S., Golub,L., and Rosner,R. 1981, ApJ 243, 288

Sheeley,N. 1980, SP 66, 79

Shimizu,T., Tsuneta,S., Acton,L.W., Lemen,J.R., Uchida,Y. 1992, PASJ, L147

Spicer,D.S. 1991, in P.Ulmschneider, E.R.Priest, and R.Rosner (eds.), *Mechanisms of Chromospheric and*

Coronal Heating, Berlin:Springer, p.547

Vlahos,L., Georgoulis,M., Kluiving,R., and Paschos,P. 1995, Astron.Astrophys. 299, 897

Vourlidas,A. and Bastian,T.S. 1996, ApJ 466, 1039

Vourlidas,A., Bastian,T.S., Nitta,N., and Aschwanden,M.J. 1996, SP 163, 99

Vourlidas,A., Bastian,T.S., and Aschwanden,M.J. 1997, ApJ 489, 403

Wragg,M.A. and E.R.Priest 1982, SP 80, 309

Wragg,M.A. and E.R.Priest 1982, AA 113, 269

Zirker,J.B. 1993, SP 148, 43

Table 1. Physical Parameters of 30 Coronal Loops (1996-Aug-29, EIT 171 Å)

Loop #	Heliographic coordinates l_1, b_1 [deg]	Azimuth angle α [deg]	Inclination angle ϑ [deg]	Emission measure EM_{max} log[cm^{-3}]	Loop width w [Mm]	Electron density n_e [10^9 cm^{-3}]	Scale height λ [Mm]	Scale height temperature T_e^λ [MK]	Filter ratio temperature T_e^{EIT} [MK]
1	247.9, -15.4	15± 1	-42± 1	27.71	6.8	2.5	49	1.08± 0.07	1.25± 0.09
2	247.7, -15.5	13± 1	-49± 5	27.93	6.1	2.3	50	1.09± 0.12	1.27± 0.10
3	247.4, -15.6	12± 1	-34± 1	27.79	7.4	2.1	57	1.25± 0.13	1.22± 0.10
4	247.3, -15.0	8± 2	-26± 1	27.60	6.9	2.6	57	1.26± 0.14	1.27± 0.11
5	247.1, -14.9	8± 3	-49± 1	27.34	6.3	2.5	56	1.22± 0.33	1.23± 0.10
6	247.0, -13.9	2± 2	-56± 1	29.68	7.0	3.7	42	0.93± 0.08	1.30± 0.12
7	246.1, -14.7	4± 2	-36± 1	27.88	7.1	1.7	62	1.36± 0.17	1.19± 0.09
8	245.2, -14.7	9± 2	-33± 2	27.45	7.1	2.2	57	1.26± 0.10	1.23± 0.06
9	247.0, -12.2	-3± 3	-12± 1	27.52	8.1	2.1	60	1.32± 0.53	1.15± 0.03
10	245.8, -13.3	1± 2	-23± 1	27.49	7.9	1.4	53	1.16± 0.30	1.21± 0.11
11	244.9, -12.2	1± 3	-31± 2	27.11	6.8	1.6	66	1.44± 0.18	1.20± 0.09
12	247.3, -10.7	-6± 2	10± 1	27.56	7.8	2.0	60	1.31± 0.07	1.10± 0.06
13	250.6, -10.1	-9± 7	11± 1	27.41	6.4	1.8	60	1.31± 0.17	1.21± 0.11
14	247.1, -9.8	-8± 3	10± 1	27.18	6.4	1.7	33	0.73± 0.08	1.12± 0.05
15	247.5, -9.0	-8± 1	12± 1	27.48	6.8	2.0	47	1.04± 0.08	1.18± 0.09
16	248.1, -8.5	-11± 3	25± 1	27.28	6.7	1.4	53	1.15± 0.32	1.24± 0.12
17	248.5, -8.0	-14± 4	32± 1	27.04	7.4	1.7	47	1.03± 0.30	1.18± 0.04
18	249.0, -7.4	-9± 4	40± 3	26.90	5.6	1.1	93	2.03± 0.41	1.30± 0.06
19	249.6, -6.9	-18± 3	39± 1	27.28	7.9	1.3	65	1.43± 0.17	1.18± 0.04
20	250.7, -6.6	-24± 6	52± 6	27.43	7.7	1.8	56	1.22± 0.05	1.22± 0.04
21	251.5, -6.1	-21± 6	58± 3	27.51	7.6	2.1	45	0.98± 0.11	1.15± 0.04
22	251.9, -5.7	-25± 5	58± 3	27.32	7.2	1.0	58	1.27± 0.82	1.22± 0.12
23	259.1, -10.7	175± 4	0± 1	27.61	8.0	2.3	60	1.31± 0.28	1.23± 0.15
24	258.6, -11.4	178± 4	14± 6	28.29	8.7	1.3	64	1.41± 0.22	1.20± 0.08
25	263.2, -16.6	178± 5	43± 1	27.38	8.1	1.8	42	0.93± 0.04	1.18± 0.11
26	259.9, -13.8	171± 4	13± 2	26.95	5.1	1.4	59	1.30± 0.36	1.15± 0.08
27	259.1, -13.4	177± 3	50± 2	27.20	7.1	1.5	58	1.26± 0.30	1.21± 0.07
28	258.0, -13.4	179± 2	27± 2	27.79	7.5	2.6	57	1.24± 0.05	1.12± 0.04
29	257.9, -13.7	185± 2	36± 1	27.76	6.0	2.4	60	1.31± 0.06	1.36± 0.07
30	257.5, -13.8	177± 3	69± 1	29.48	7.4	1.7	38	0.84± 0.10	1.16± 0.08
average	251.0, -11.8	-3±10	7±37	27.61± 0.61	7.1±0.8	1.9±0.6	55± 10	1.22± 0.23	1.21± 0.06

Fig. 1.— SoHO/EIT Fe IX/X image of active region AR 7986, recorded on 1996-Aug-30, 0020:14 UT, at a wavelength of 171 Å, sensitive in the temperature range of $T_e = 1.0 - 1.5$ MK (top). The greyscales of the image is scaled logarithmically in flux, the contours correspond to increments of 100 DN (data numbers). The heliographic grid has a spacing of 5^0. The filtered image (lower panel) was created by subtracting a smoothed image (using a boxcar of 3×3 pixels) from the original image, in order to enhance the loop fine structure.

Fig. 2.— Definition of loop parameters: loop point positions $(x_i, y_i), i = 1, ..., n$ starting at the primary footpoint at height $h_1 = h_{foot}$, the azimuth angle α between the loop footpoint baseline and heliographic East-West direction, and the inclination angle ϑ between the loop plane and the vertical to the solar surface.

Fig. 3.— The principle of *Dynamic Stereoscopy* is illustrated here with an example of two adjacent loops, where a thicker loop is bright at time t_1, while a thinner loop is brighest at time t_2. From the loop positions (x_i, y_i) measured at an intermediate reference time t, i.e. $t_1 < t < t_2$ (middle panel in middle row), projections are calculated for the previous and following days for different inclination angles ϑ of the loop plane (left and right panel in middle row). By extracting stripes parallel to the calculated projections $\vartheta = 10^0, 20^0, 30^3$ (panels in bottom part) it can be seen that both loops appear only coaligned with the stripe axis for the correct projection angle $\vartheta = 20^0$, regardless of the footpoint displacement Δx between the two loops. The coalignment criterion can therefore be used to constrain the correct inclination angle ϑ, even for dynamically changing loops.

Fig. 4.— Projections of 30 stereoscopically reconstructed loop segments (numbered white curves) are shown overlaid on the *SoHO/EIT* 171 Å images (top panels) and the filtered images (bottom panels) of 1998-Aug-29, 30, and 31. The 30 loop segments were traced from the filter image of Aug 30 (bottom middle panel), while the projections on the previous and following day were calculated from the inclination angles ϑ obtained from the *dynamic stereoscopy* method. Note that the overall magnetic field structure is almost invariant during the 3 days, but dynamic changes of the loops produce slight displacements between the calculated projections forward and backward in time and the actually observed fine structure.

Fig. 5.— Three different projections of the stereoscopically reconstructed 30 loops of AR 7986 are shown. The loop segments that were traced from the 96-Aug-30 171 Å image are marked with thick solid lines, while the extrapolated segments (marked with thin solid lines) represent circular geometries extrapolated from the traced segments. The three views are: (1) as observed from Earth with l_0, b_0 (bottom right panel), (2) rotated to North by $b'_0 = b_0 - 100^0$ (top right panel), and (3) rotated to East by $l'_0 = l_0 + 97.2^0$ (corresponding to -7.2 days of solar rotation; bottom left panel). An *EIT* 171 Å image observed at the same time (-7.2 days earlier) is shown for comparison (top left panel), illustrating a similar range of inclination angles and loop heights as found from stereoscopic correlations a week later. The heliographic grid has a spacing of 5^0 degrees or 60 Mm.

Fig. 6.— The positions of the curved coordinate grids of the 30 analyzed loop segements are shown in the top right panel, which has the same orientation as the 1996-Aug-30 map shown in Fig.4 (middle). The coordinate grid of loop #1 is represented with 1-pixel resolution, while only the outer borders and central axes are indicated for the other loop segments. - The vertically oriented panels represent the coordinate grids of the analyzed 30 loops, stretched out along the loop axis. The top of the panels corresponds to the primary footpoint (see positions l_1, b_1 in Table 1). In each panel we show the EIT 171 Å flux loop cross-sections measured perpendicularly to the loop axes. Successive cross-sections are separated by a distance of 1 pixel along the loop axis. The flux associated with each loop is marked with a grey area, obtained by background subtraction with a cubic spline interpolation between both sides of the loop cross-section.

Fig. 7.— The loop-associated EUV flux ($F_{loop}(s)$, thick line), the total EUV flux ($F_{total}(s)$, thin line), and the background ($F_{total}(s) - F_{flux}(s)$, dotted line) measured along the loop is shown for Loop #1 (left panel). A histogram of the relative fractions F_{loop}/F_{total} (integrated over the traced loop lengths) is shown from all 30 analyzed loops in right panel.

Fig. 8.— The variation of the loop thickness is shown for the 10 loops with the least confusion by adjacent loops (see cross-sections in Fig.6) as function of the loop length s (left panels). A linear regression fit is indicated (solid line in left panels). The average (equivalent) width w is histogrammed for all 30 analyzed loops (top right). A loop divergence factor is calculated from the ratio of the average width in the upper half and lower half (traced) loop segments (right bottom). Note that most of the loops show no significant loop thickness variation.

Fig. 9.— Left panel: The effect of the variable column depth $w_z(s)$ measured parallel to the line-of-sight z is illustrated as function of the loop length parameter s, for a loop with a constant diameter w. Right panel: The effect of the inclination angle ϑ of the loop plane on the inferred density scale height $\lambda(\vartheta)$ is shown. Both effects have to be accounted for the determination of the electron density $n_e(s)$ along the loop.

Fig. 10.— The electron density $n_e(s)$ (left panels) and the EIT filter-ratio electron temperature $T_e(s)$ (right panels) as function of the loop length s for the same 10 loops selected in Fig.8. An exponential model $n_e(h)$ is fitted, yieling the density scale height λ and scale height temperature T_e^λ indicated in the left panels. The average EIT filter-ratio temperature T_e^{EIT} (obtained from 171/195 Å images) is indicated in the right panels. A temperature gradient dT_e/ds is listed if the gradient is significant.

Fig. 11.— Statistics of scale height temperatures T_e^λ (left top panel), EIT filter-ratio temperatures T_e^{EIT} (left bottom panel), scatter plot of these two temperatures (right top panel), and EIT temperature gradients dT/ds (right bottom panel) for all analyzed 30 loops.
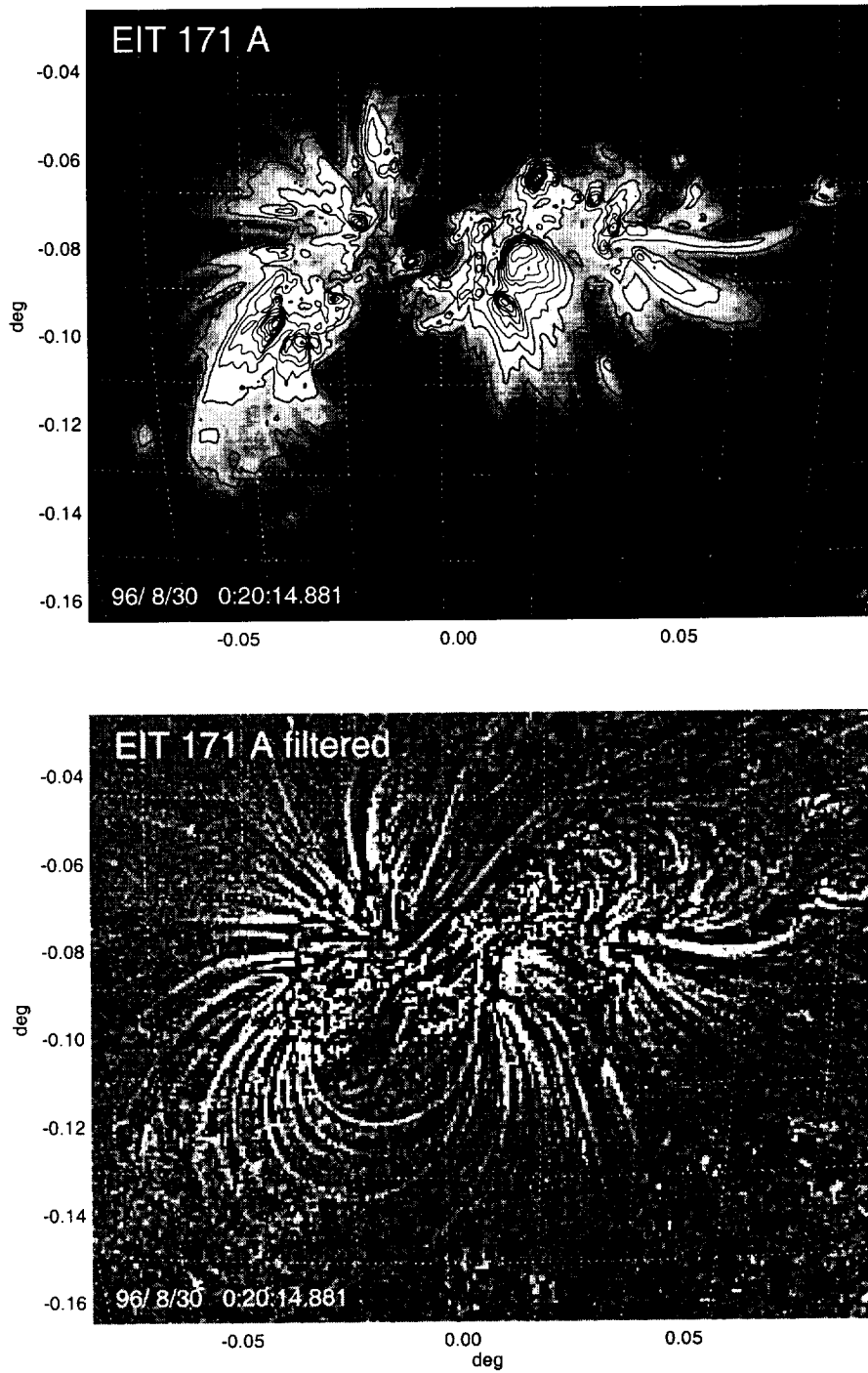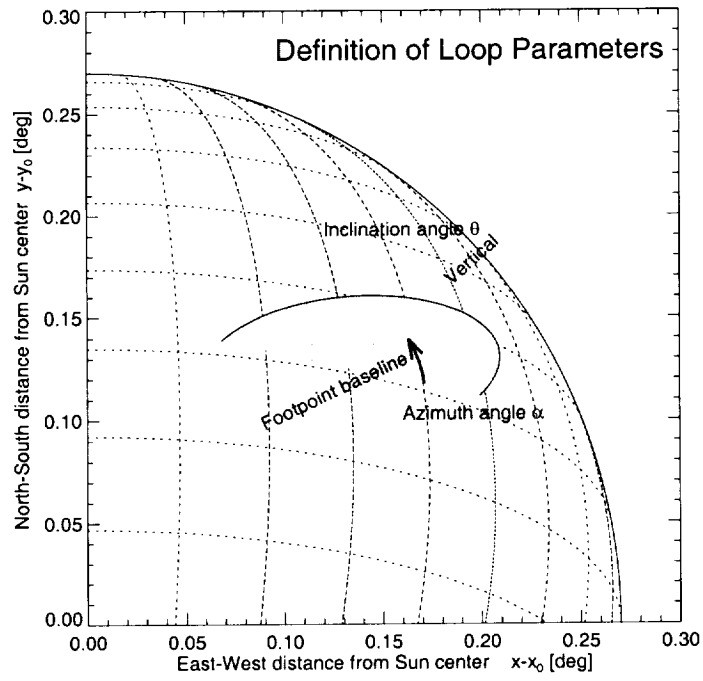
Fig. 12.—

EIT 171 A

96/ 8/30   0:20:14.881

EIT 171 A filtered

96/ 8/30   0:20:14.881

Figure 1 : AR 7986 (Aschwanden et al. 1998)

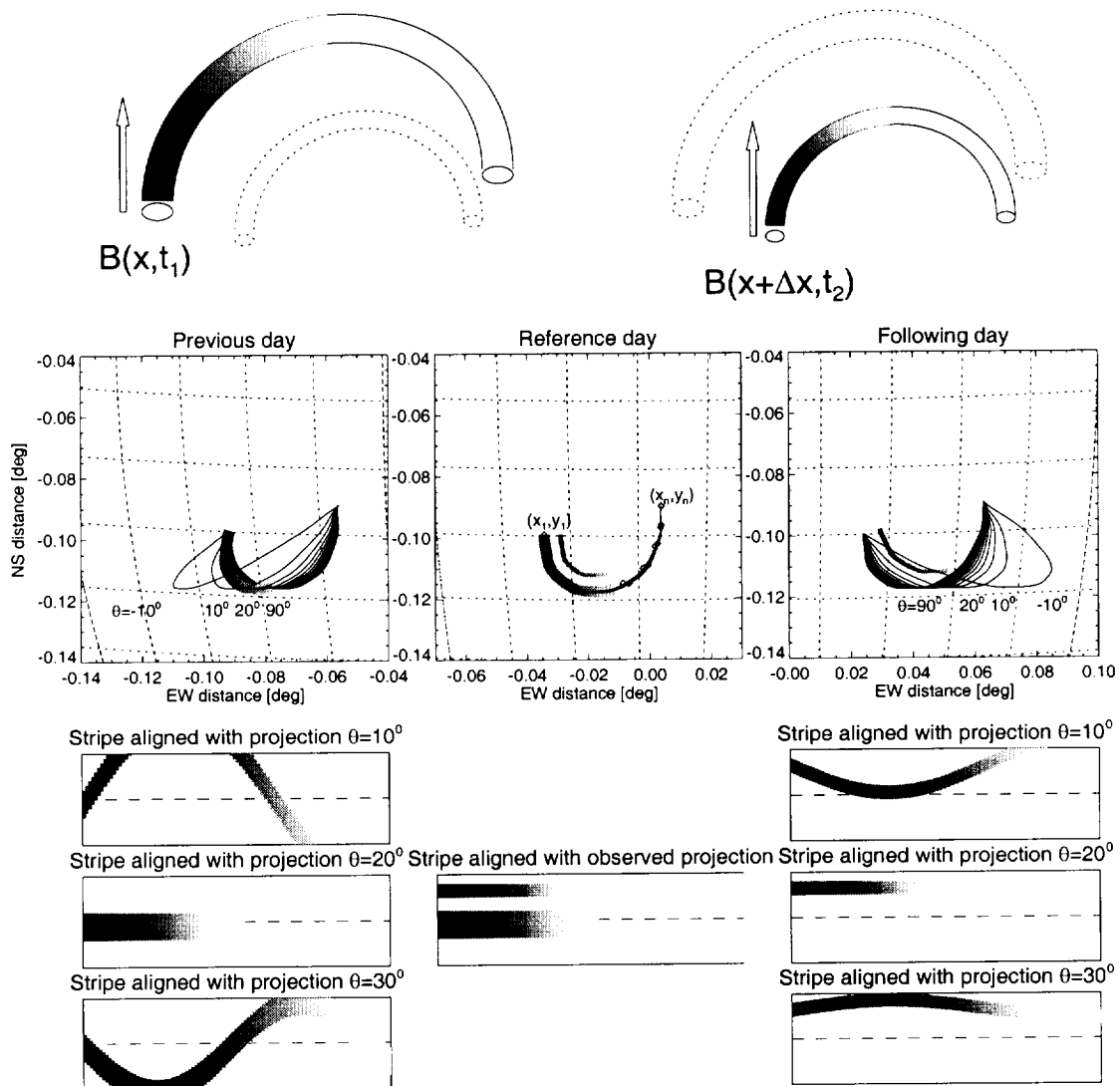Figure 2 : AR 7986 (Aschwanden et al. 1998)

Principle of Dynamic Stereoscopy

$B(x,t_1)$

$B(x+\Delta x, t_2)$

Previous day

Reference day

Following day

Stripe aligned with projection $\theta=10^\circ$

Stripe aligned with projection $\theta=10^\circ$

Stripe aligned with projection $\theta=20^\circ$ Stripe aligned with observed projection Stripe aligned with projection $\theta=20^\circ$

Stripe aligned with projection $\theta=30^\circ$

Stripe aligned with projection $\theta=30^\circ$

Figure 3 : AR 7986 (Aschwanden et al. 1998)
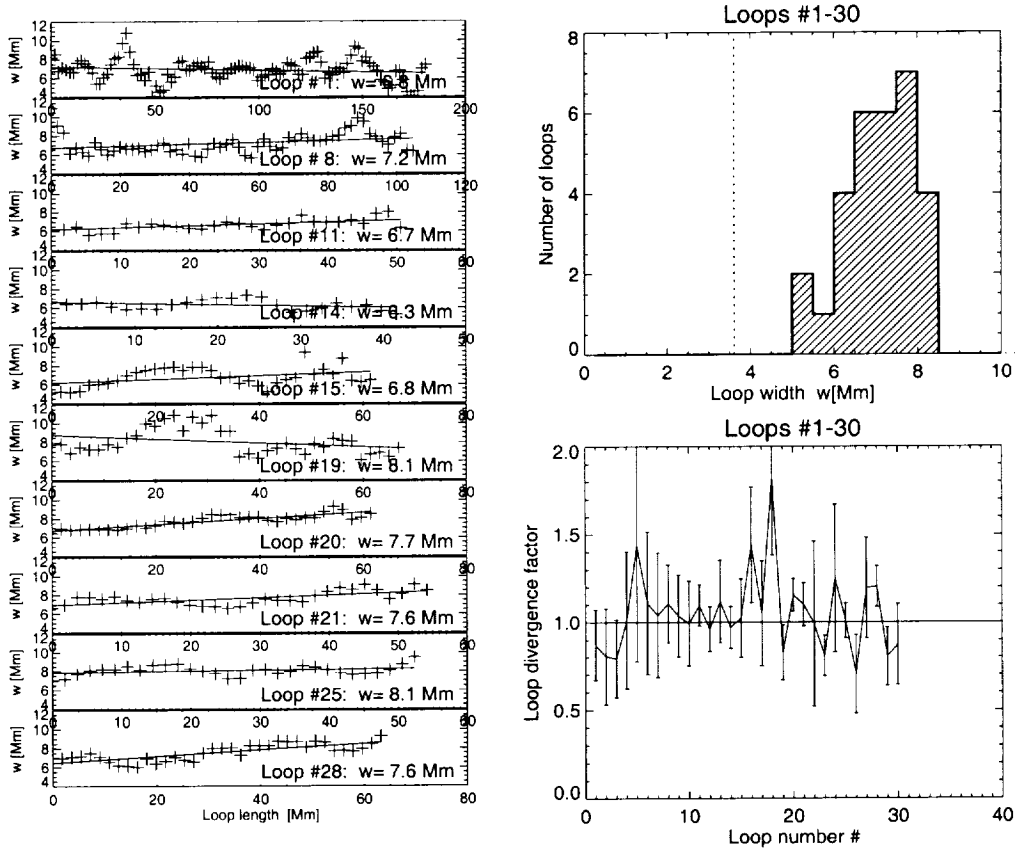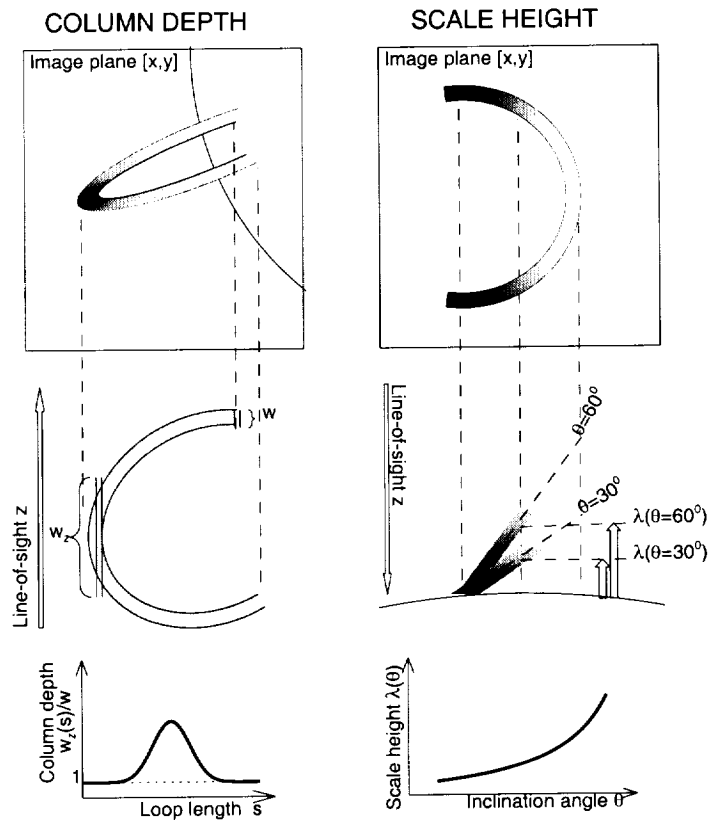
1996-Aug-29

1996-Aug-30

1996-Aug-31
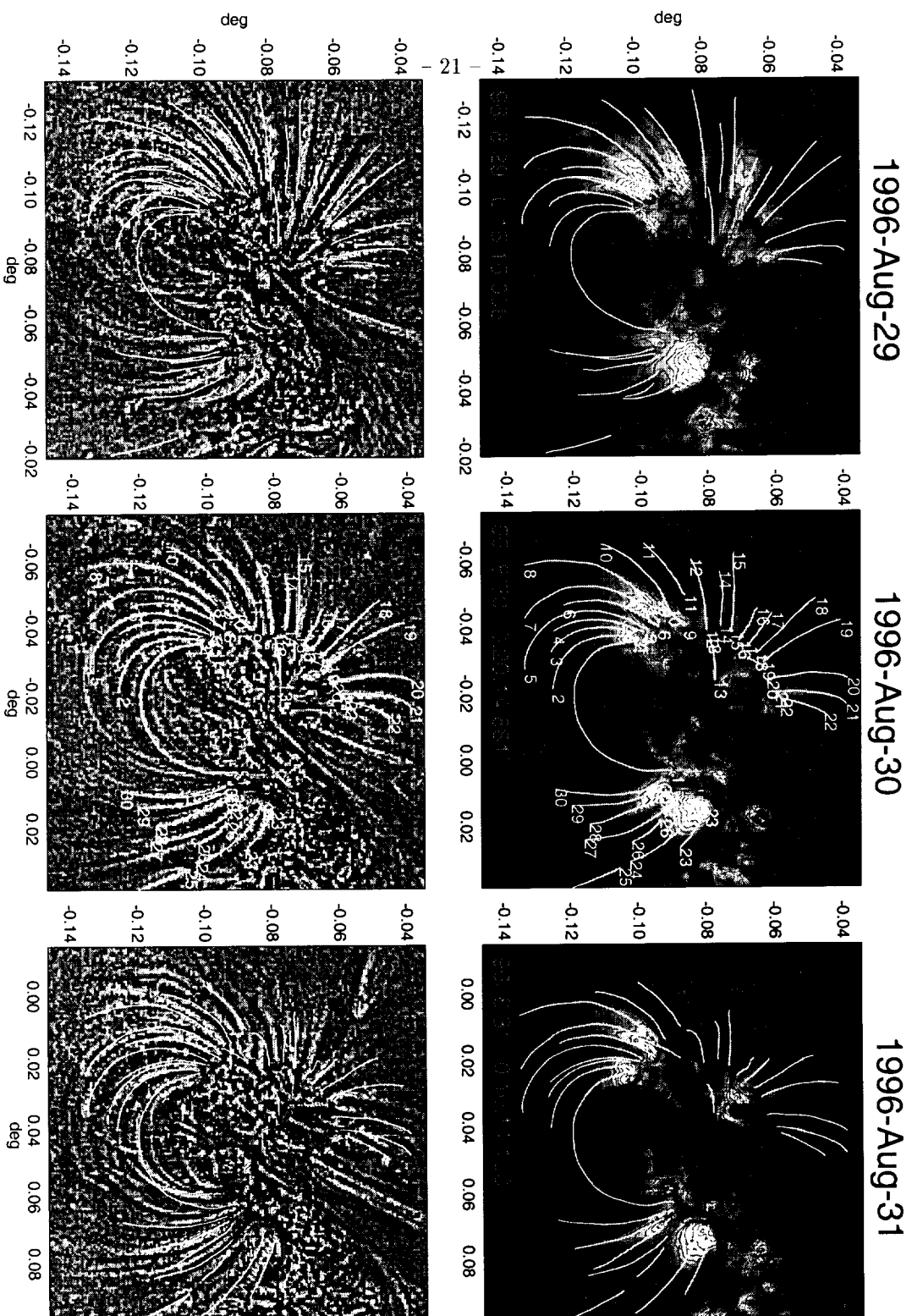
Figure 4 : AR 7986 (Aschwanden et al. 1998)
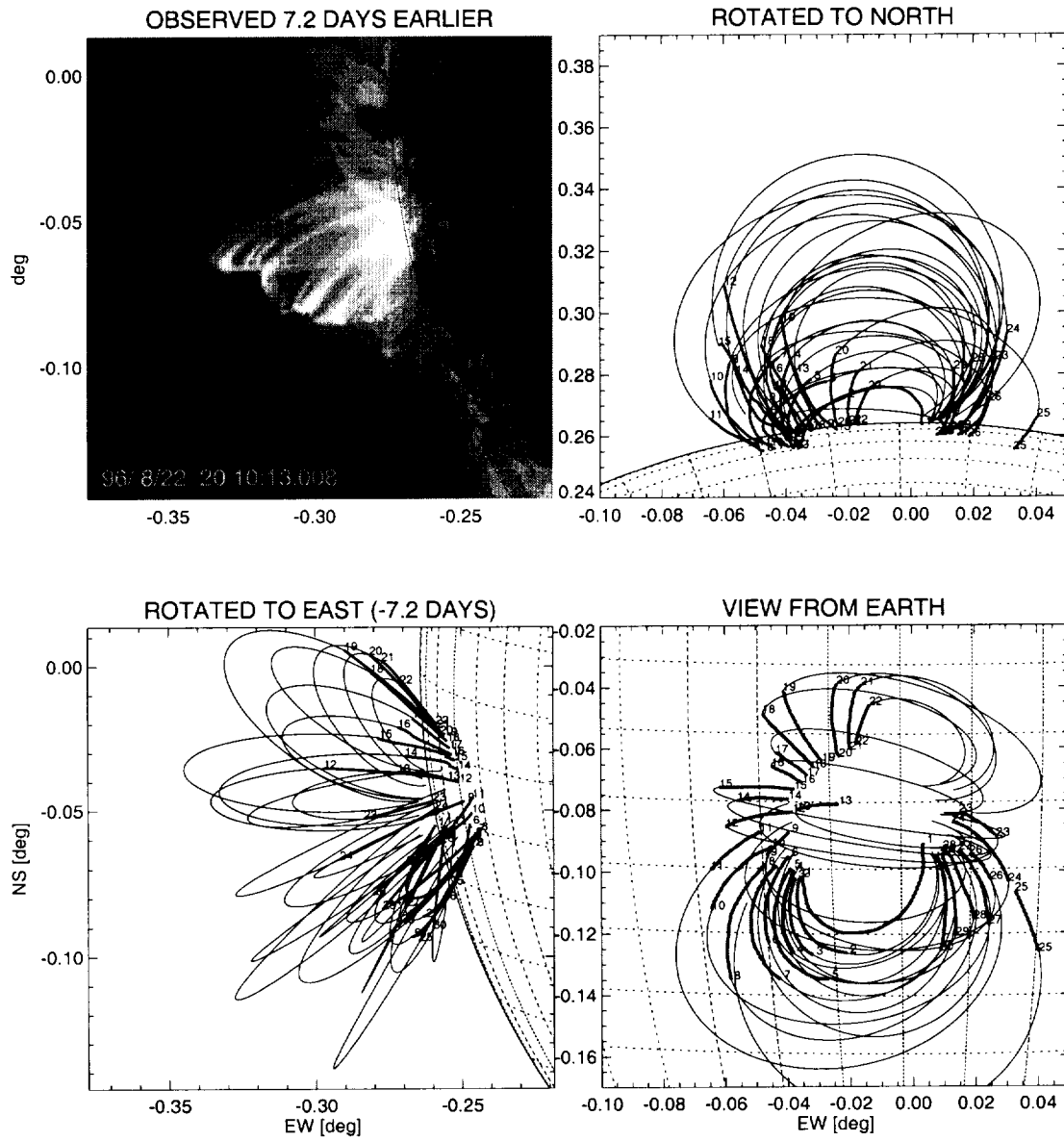
Figure 5 : AR 7986 (Aschwanden et al. 1998)
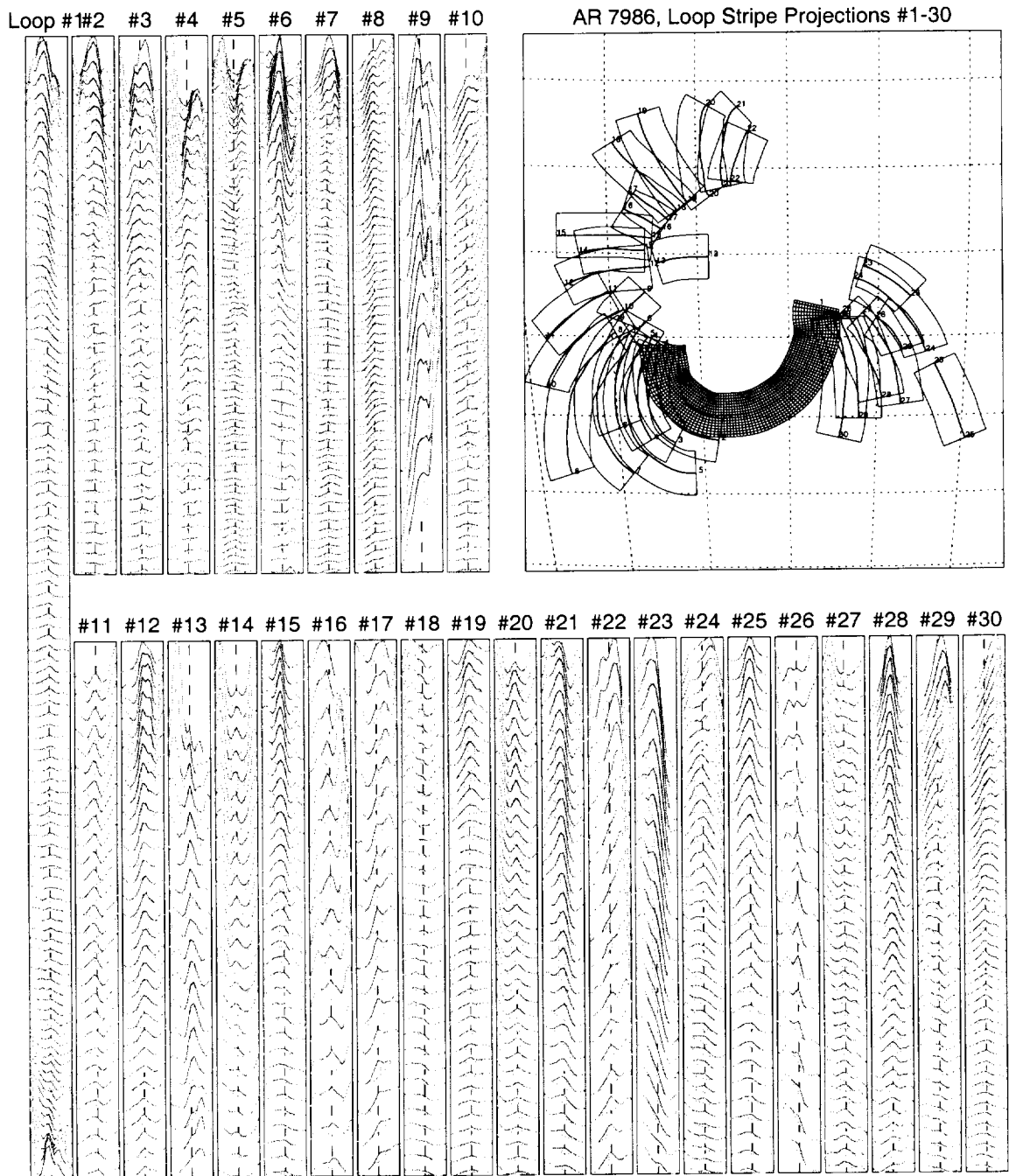
Figure 6 : AR 7986 (Aschwanden et al. 1998)
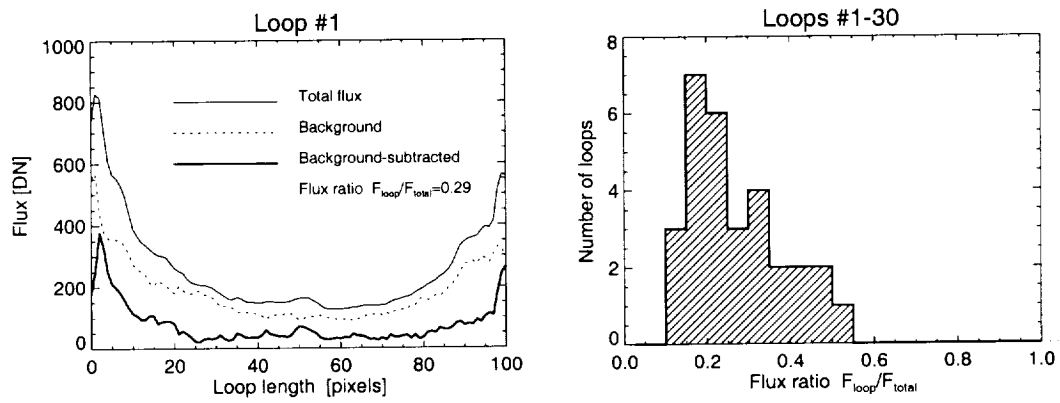
Figure 7 : AR 7986 (Aschwanden et al. 1998)

Figure 8 : AR 7986 (Aschwanden et al. 1998)

COLUMN DEPTH SCALE HEIGHT
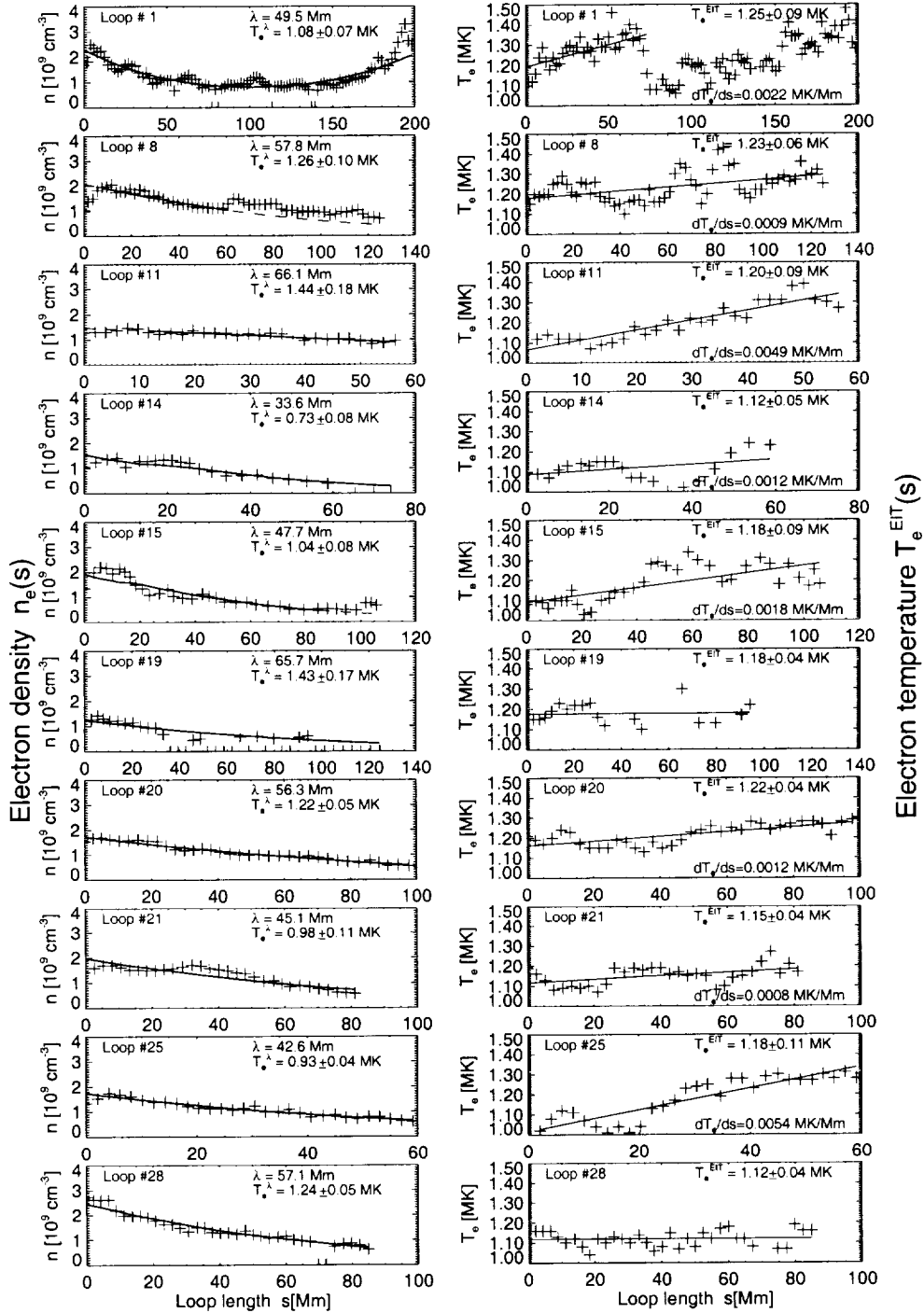

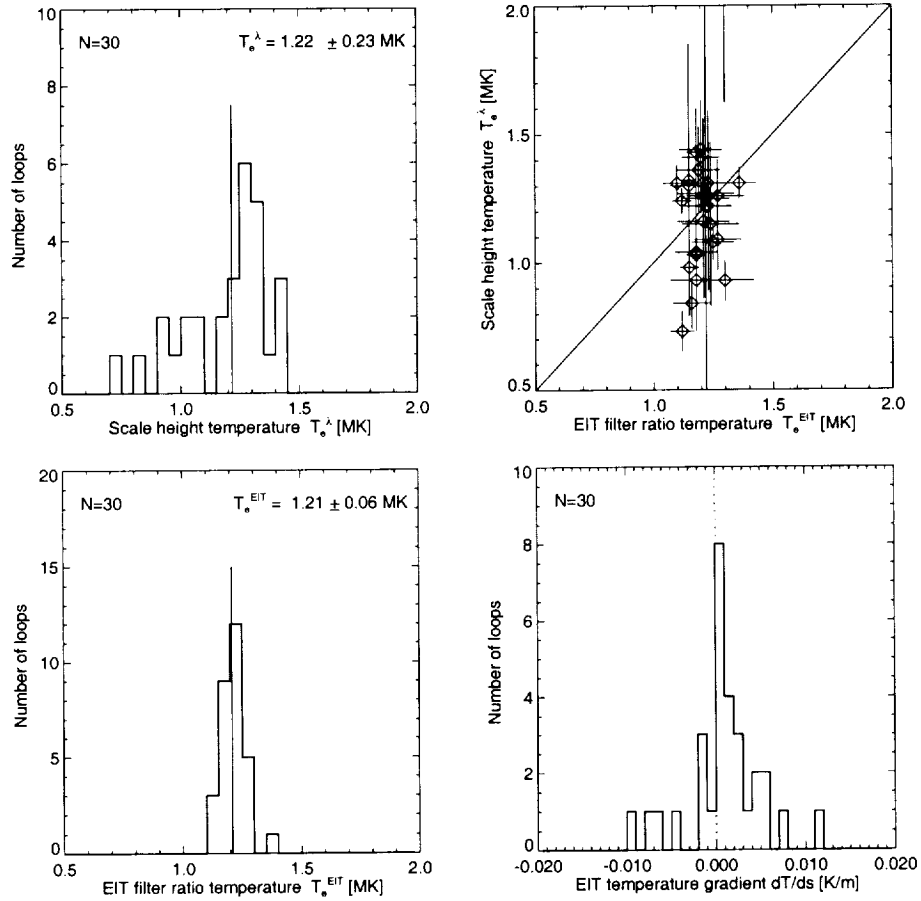Figure 9 : AR 7986 (Aschwanden et al. 1998)

Figure 10 : AR 7986 (Aschwanden et al. 1998)

Figure 11 : AR 7986 (Aschwanden et al. 1998)